Cell Reports
Physical Science

CellPress
OPEN ACCESS

Report

Geometry-preserving expansion microscopy microplates enable high-fidelity nanoscale distortion mapping

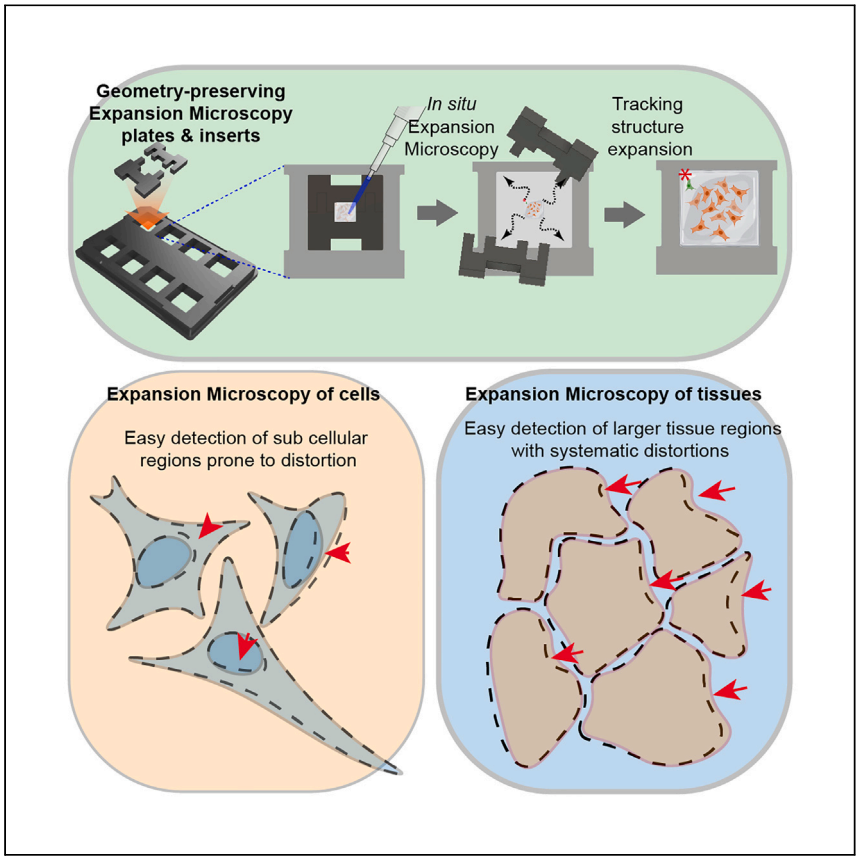

Expansion microscopy is an analytical protocol that allows the physical magnification of biological structures (cells, tissues, and organisms) with swellable hydrogels. Seehra et al. report the development of an array-based approach to containing gel expansion and visualization of spatial distortions intrinsic to magnified cell and tissue ultrastructure.

Rajpinder S. Seehra, Samantha J. Warrington, Benjamin H.K. Allouis, ..., Daniel Bose, David Strutt, Izzy Jayasinghe

i.jayasinghe@sheffield.ac.uk

Highlights

3D-printed microplate system designed for *in situ* ExM

Plate-based ExM avoided handling and preserved gel geometry during expansion

Pre- and post-ExM imaging within each well allowed visualization of distortions

Distortions observed in sub-cellular areas in HeLa cells and across fly wing tissue

Seehra et al., Cell Reports Physical Science 4, 101719
December 20, 2023
https://doi.org/10.1016/j.xcrp.2023.101719

Cell Reports
Physical Science

CellPress
OPEN ACCESS

Report

Geometry-preserving expansion microscopy microplates enable high-fidelity nanoscale distortion mapping

Rajpinder S. Seehra,[1] Samantha J. Warrington,[1] Benjamin H.K. Allouis,[1] Thomas M.D. Sheard,[1] Michael E. Spencer,[1] Tayla Shakespeare,[1] Ashley Cadby,[2] Daniel Bose,[1] David Strutt,[1] and Izzy Jayasinghe[1,3,4,*]

SUMMARY

Expansion microscopy (ExM) is a versatile super-resolution microscopy pipeline, leveraging nanoscale biomolecular crosslinking and osmotically driven swelling of hydrogels. Currently, ExM is a laborious and skill-intensive technique, involving manual handling of the hydrogels that can compromise the integrity of the gels and capacity to track gel isotropy, hence diminishing reproducibility. We have developed a 3D-printable microplate system to contain the entire ExM workflow within each well, enabling *in situ* image acquisition and eliminating the need for direct handling of the hydrogels. The preservation of the gel geometry and orientation of the microplate wells enables convenient tracking of gel expansion, pre- and post-ExM image acquisition, and distortion mapping of every cell or region of interest. We demonstrate the utility of this approach with both single-color and multiplexed ExM of cultured HeLa cells and dissected pupal *Drosophila melanogaster* wing tissue to reveal distortion-prone structures ranging from sub-cellular organelles to micron-scale tissue regions.

INTRODUCTION

Super-resolution microscopy methods have considerably shifted the capabilities of optical bioimaging, from cellular or sub-cellular scales to the true molecular scale. While the conventional stochastic (e.g., STORM, PALM, and PAINT) and deterministic (e.g., 4Pi, STED, and SIM) approaches to super-resolution have pioneered many of the breakthroughs in this technology, access to the specialist optical instruments and mastery of the underpinning photochemistry continue to limit their uptake. Expansion microscopy (ExM) has offered a radically different strategy to achieving super-resolution.[1] By combining molecular crosslinking chemistries with osmotically swellable polyacrylamide hydrogels, ExM enables the *physical* magnification of the ultrastructure. Super-resolution can therefore be achieved through fluorescence imaging of an inflated facsimile of the structure with relatively conventional (e.g., confocal) imaging systems.

The utility of ExM has grown with the development of a range of ExM recipes, each with improvements in (1) accessibility of key reagents and components,[2] (2) expansion factor toward greater resolution,[3,4] (3) isotropy of gel expansion toward higher-fidelity sample expansion,[4–6] and/or (4) compatibility with different sample species,[7] biomolecules,[8] constituents,[9] and sample formats.[10] Combining of ExM chemistries

[1]School of Biosciences, Faculty of Science, The University of Sheffield, Sheffield S10 2TN, UK

[2]Department of Physics and Astronomy, The University of Sheffield, Sheffield S10 3RH, UK

[3]EMBL Australia Node in Single Molecule Science, Department of Molecular Medicine, School of Medical Sciences, UNSW Sydney, Kensington, Sydney, NSW 2052, Australia

[4]Lead contact

*Correspondence: i.jayasinghe@sheffield.ac.uk

https://doi.org/10.1016/j.xcrp.2023.101719

with established super-resolution modalities has given rise to ExM variants such as ExSTED,[11] ExSIM,[12] ExSMLM/Ex*d*STORM,[13] EExM,[14,15] and one-nanometer expansion microscopy,[16] allowing users to compound the resolution gain between the optical, computational, and hydrogel enhancements. Finally, the rapidly growing range of molecular probes and staining protocols,[9,17] particularly the adaptation of fluorescent dye esters as nondescript counter stains,[18,19] have also made ExM a highly versatile route to super-resolution microscopy.

Despite the variations of ExM, the workflow of sample preparation remains highly reliant on manual handling of the gel and user skill, particularly from the gelation to image acquisition stages.[20] Of note, the method involves repeated manual handling of the gel during the transfer, osmotic swelling, and trimming of the gel blocks. Skill is essential to minimize distortion, damage, and/or tearing of the hydrogels and the structures imprinted within. Further to this, spatial heterogeneities in the gel matrix, proteolytic digestion, and intrinsic stiffness within the sample are known to give rise to anisotropies in the gel expansion.[15,21] The same phenomena can also give rise to sample-to-sample and region-to-region variations in expansion factor, usually measured by changes in the overall gel dimensions.[14] Additional strategies include, embedding DNA origami calibrants,[6] using biological structures and shapes intrinsic to the samples (e.g., nuclear pore complexes[22] or muscle sarcomeres[14]), patterned fluorescence photobleaching,[23] and gridded substrates that impart trackable imprints on the gel.[24] Nevertheless, imaging the same regions or structure at the pre- and post-expansion states[25] remain the gold standard for assessing expansion factor and any distortions. Due to the manual nature of the gelation and gel expansion steps, sequential pre- and post-ExM imaging currently remains a skilled and time-consuming mode of ad hoc validation.

Array-based ExM promises to remove or reduce the manual handling of the hydrogels and add scalability to this method as demonstrated by a pioneering study by Day et al., which uses traditional 96-well plates.[26] Aside from this demonstration, ExM remains a low-throughput imaging modality. In this paper, we present the adoption of three-dimensional (3D) printing and rapid prototyping as a strategy to develop a bespoke microplate-based ExM protocol that also preserves hydrogel geometry and orientation to enable trackable, pre- and post-ExM imaging of every sample and region of interest.

RESULTS AND DISCUSSION

3D-Printable, geometry-preserving ExM microplate

ExM is commonly achieved through a series of chemical anchoring, gelation, digestion, and expansion steps of a fluorescently stained sample (Figure 1A). In its typical implementation, coverslips containing cell or tissue samples are manually lowered onto an aqueous mix of gel monomers, polymerization catalysts, and initiators. The polymerized gel may be transferred to a chamber or plate for the proteolytic digestion and washes, and then transferred again to a large Petri dish for the osmotic swelling in the expansion stage. Expanded gels are trimmed to fit the size of an imaging chamber before being placed on the microscopes. The latter three steps each involve manual handling and transfer of the gel. Skill, experience, and time are essential to ensure that the integrity and isotropy of the sample are preserved.[25]

We developed a 3D-printable, 8-well microplate and a set of silicone frame inserts to perform ExM within each well without having to remove the gel or the sample at any stage of the protocol (Figure 1B; the design model is included in the data supplement—see data and code availability for details). Each well was a 2 × 2-cm square

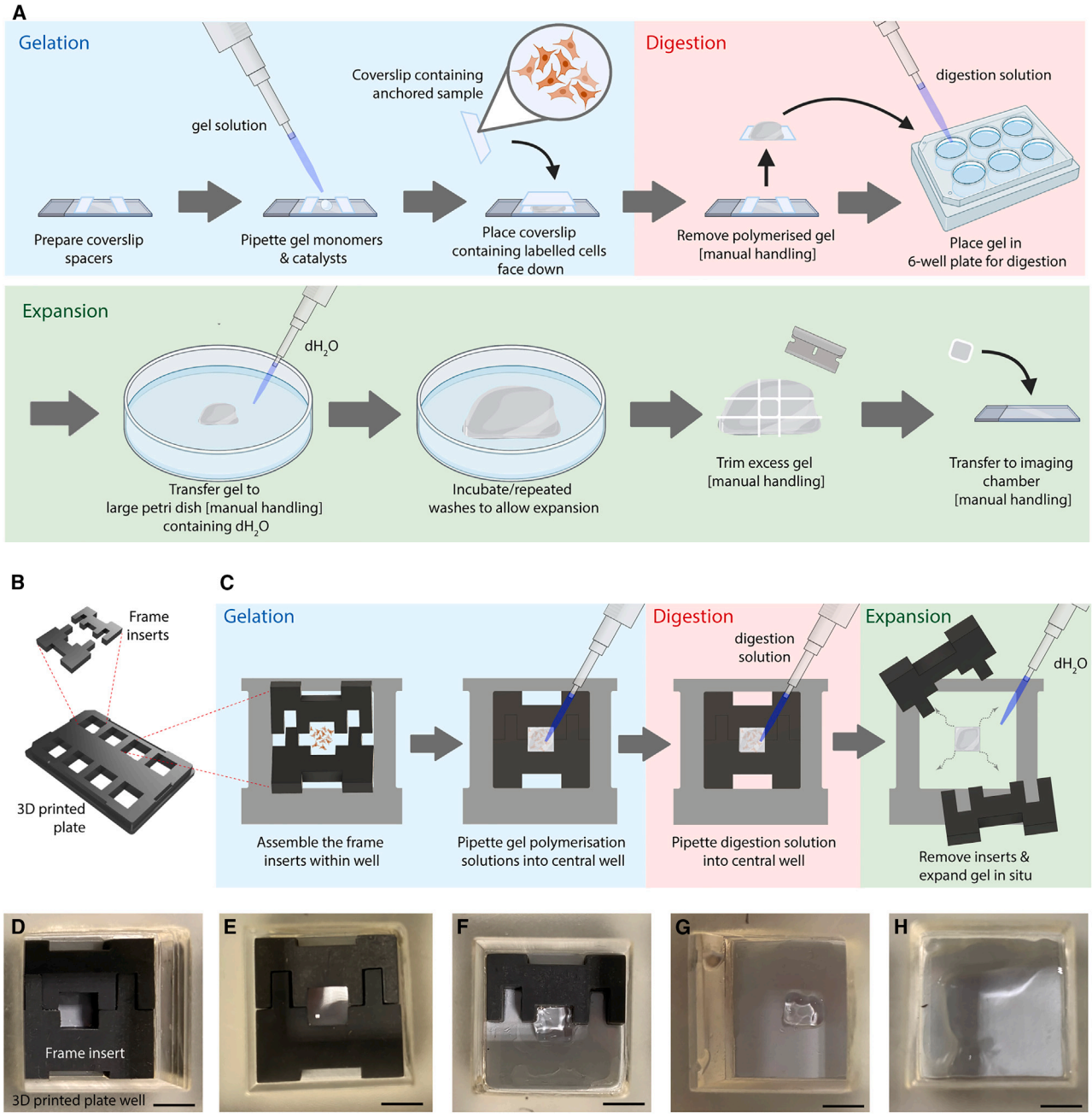

Figure 1. Conventional and microplate-based implementation of ExM

(A) The conventional ExM protocol involves the three main stages of ExM, gelation, digestion, and expansion. Manual handling and/or transfer of the gel is likely in the post-gelation, post-digestion, and post-expansion stages.

(B) The design of a 3D-printable microplate, consisting of eight square wells and a pair of silicone frame inserts, which assembles into each well.

(C) In the microplate-based ExM workflow, the frame inserts are pushed to the bottom of the well either prior to seeding the cells in the central region of the well or following immunostaining. The gel polymerization and digestion steps take place within the central well. The frame inserts are removed to release the square-shaped gel prior to the expansion step. Carefully adding deionized water (dH_2O) allows the gel to expand 4× to fill the main well. Shown, are a series of photographs of: (D) the assembly of inserts in the well, (E) the forming of the gel within the central gel casting well, (F) the releasing of the gel from the frame inserts, (G) the released gel (pre-expansion), and (H) the expanded gel filling the overall well. Note, excess liquid has been removed from the wells for clarity of the photographs. Scale bars, 5 mm.

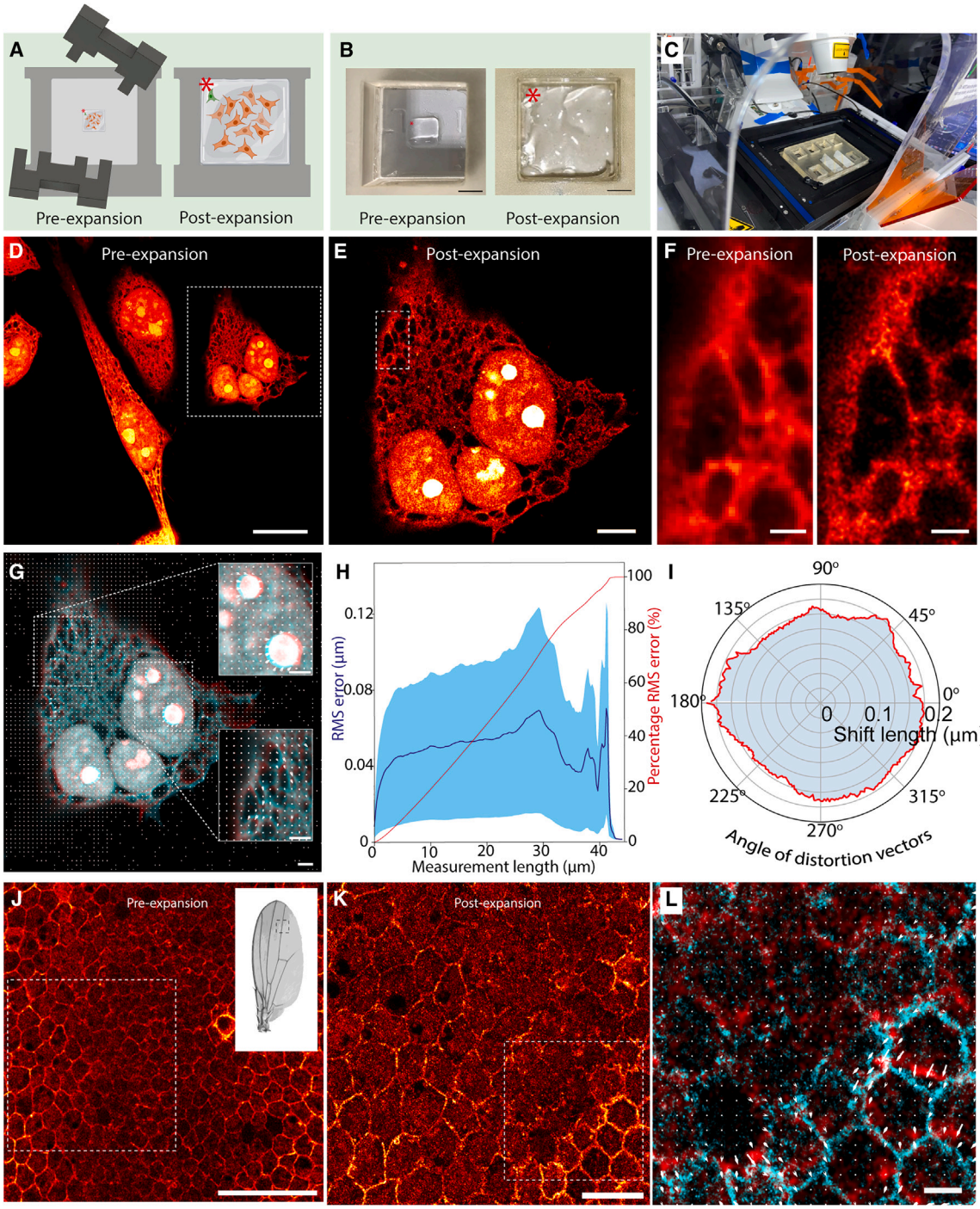

Figure 2. ***In situ*, pre- and post-ExM imaging and sub-cellular and tissue-wide distortion assessment**

(A) Schematic diagram and (B) photographic illustrations of the square shape of the gel released from the frame inserts (left) and the gel following 4× *in situ* expansion filling the well (right). The preservation of the geometry and orientation of the gel means that the upper right corner of the sample within the casting well moves unambiguously to the upper right corner of the overall well (red asterisk).

(C) The coverslip bottoms of each well and the standardized base of the microplate allows it to be seated directly on a Zeiss Airyscan LSM880 microscope for imaging into the gels at pre- and post-ExM stages.

(D) A pre-ExM image of HeLa cells stained with an AZ488 NHS ester.

(E) Post-ExM Airyscan image of the boxed region in (D).

(F) Magnified and re-scaled view of the region shown within the dashed lines in (E) at pre-ExM (left) and post-ExM (right) stages.

Figure 2. *Continued*

(G) Aligned and scaled overlay of the pre-ExM (red) and post-ExM (cyan) Airyscan images of the cell and the local distortion map between the post- and pre-ExM images (white arrows). The insets show magnified regions within the nucleoplasm and near cell periphery, marked by the dashed lines, featuring longer distortion vectors representing local distortions. See Figure S1 for a high-resolution view of this panel.

(H) Mean RMSE observed across five image datasets plotted against the length scale across which the distortions are detected (solid blue line; shaded area indicates standard deviation). The cumulative normalized RMSE (red line) is shown as an overplot as a function of the measurement length scale.

(I) Polar plot of the average distortion vectors (radial axis) against directionality (angular axis) for the image area presented in (G).

(J) Pre-expansion image of *shg*:E-cad-GFP pupal wing tissue stained with anti-GFP antibody; drawing of the inset illustrate the approximate region of the wing imaged.

(K) Image of the box region shown in (J), acquired following 4× ExM.

(L) Aligned and scaled overlay of the pre-ExM (red) and post-ExM (cyan) Airyscan images of the local distortion map between the post- and pre-ExM images (white arrows) in the boxed region in (K). Scale bars, 5 mm (B), 20 μm (D), 5 μm (E), 1 μm (F), 2 μm (G), 50 μm (J), 20 μm (K), and 5 μm (L).

chamber and a no. 1.5 glass coverslip bottom to allow direct imaging from underneath. Cells could either be cultured within the central portion of each well or the inserts may be placed after the cells were cultured and fixed *in situ* (Figure 1C). In the latter approach, it was important to blot away any residual liquid from the edges of the well to allow the silicone frame inserts to form a dry seal when pressed into the well. Similar to a jigsaw, each pair of frame inserts was assembled and seated within the chamber to form a vacant central region either before adherent cells were seeded or following the staining and anchoring steps. The central well (a 0.5 × 0.5-cm square) formed by the frame acted as the casting well for the hydrogel. Once polymerized, the digestion solution and subsequent wash buffers could be pipetted into the same well. The frame was dismantled by leveraging tweezers gently against the chamber walls and removed from the well. Provided that the frame inserts formed a substantial seal against the dry portions of the coverslip, this step should leave a square gel block at the center of the well; if not, careful scoring of the gel along the edge of the central well with a sharp scalpel was necessary prior to the release of the gel block. To allow the square gel to expand, deionized water (dH_2O) was gently pipetted into the same well taking care to prevent the gel from rotating. The protein-retention ExM[2] formula of the gel allowed it to expand to ~4 times to fill the square space defined by the well. Figures 1D–1H are a sequence of photographs of the steps in performing ExM on HeLa cells cultured and fixed within a chamber. A 3D-printable lid (included in data supplement—see data and code availability for details) was also designed; however, lids of standard 98- or 6-well microplates were also compatible with our bespoke microplate.

The square geometry into which the gel is cast, along with the square shape of each well, allowed us to maintain the expanded gel in its original orientation. Therefore, a cell or tissue region of interest originating at the top left corner of the casting well could be tracked reliably to the top left corner of the overall well following expansion (red asterisks in Figures 2A and 2B). The footprint of the microplate base was designed to match the industry-standard microplates, which allowed us to conveniently seat the plate within a standard stage plate of an inverted Zeiss Airyscan LSM 880 (Figure 2C). The no. 1.5 glass coverslip bottom of each well permitted us to focus light through high-numerical aperture objective lenses directly into the samples, *in situ*, both in the pre- and post-expansion image acquisition. Pre- and post-expansion Airyscan image pairs of cultured HeLa cells stained directly with AZ488 NHS ester, an analog of Alexa Fluor 488 NHS characterized previously as an ExM counterstain,[27] demonstrated the ability to conveniently track the same regions of the sample with minimal rotation (Figures 2D and 2E).

Pre- and post-expansion image visualization and distortion analysis

This approach of pre- and post-ExM re-imaging enabled two principal modes of data visualization. Firstly, it was straightforward to *directly* compare the

super-resolution image with the diffraction-limited standard to demonstrate the resolution improvement (Figure 2F)—as is often *not* shown in ExM studies. Secondly, the images of cells could be directly scaled, registered, and subject to a 2D spatial distortion analysis. Figure 2G illustrates an overlay of the pre-expansion (red) and post-expansion (cyan) images, along with a 2D vector map of the local registration error (white arrows; see Figure S1 for high-resolution version). This analysis allowed us to recognize the boundary of the cell, particularly near the interfaces of internal compartments such as the endoplasmic reticulum (ER) and the plasmalemma of the cell, and the intra-nuclear structures as the sub-cellular regions most prone to anisotropic expansion (see magnified view in insets of Figure 2G). In addition, convenient pre- and post-expansion imaging allowed us to carry out a root mean-square error (RMSE) analysis (Figure 2H) to identify the length scales of the greatest spatial errors resulting from anisotropies or distortion on a cell-by-cell basis. It also allowed us to visualize the distortion vectors in a polar plot that reported any systematic asymmetries or directionalities in the distortions present in the region of interest. The polar plot in Figure 2I confirmed that the directionality of distortion vectors largely followed a random uniform distribution, indicative of no directional bias in the sample expansion.

In addition to imaging cells cultured within each well, we also performed 4× ExM on whole pupal *Drosophila melanogaster* wing tissue immunostained against E-cadherin-GFP (E-cad-GFP) using the microplates (Figure 2J). Figure 2K shows the post-ExM imaging of the sub-region of the wing tissue within the boxed region of Figure 2J. Scaling and registering these tissue pre- and post-ExM images and the subsequent distortion vector analysis revealed regions within the tissue, tens of micrometers in size, that contained systematic directional distortions (Figure 2L; see full analysis in Figure S2).

Two-color imaging and multi-channel distortion analysis

The 3D-printed microplate-based ExM approach further lent to multiplexed staining and imaging. Figures 3A–3D show two distinct dual-color ExM experiments carried out within microplate wells. In the first, fixed HeLa cells were stained with a nondescript AZ488 NHS ester (upper row of Figure 3A) and co-immunostained for KDEL peptide sequence found in distal ER (lower row). Shown, are the pre-ExM (Figure 3Ai), registered post-4× ExM (Figure 3Aii), and overlay Airyscan images (Figure 3Aiii) corresponding to the two labels. In addition to the visual overlays, we could examine the distortion vector maps for each imaging channel separately, accounting for any distortions arising from linkage errors unique to each label (Figure 3Aiv; high-resolution version in Figures S2 and S3). It also allowed us to recover distortion information in regions of the cell (in this example, the nucleoplasm and perinuclear regions) with the AZ488 NHS stain that were otherwise devoid of KDEL labeling. The comparison of the RMSE plots of the two channels showed that, with more widespread stains such as the AZ488 NHS ester, we can report errors in longer length scales in comparison with relatively segregated or localized targets such as KDEL (Figures 3A, v). A split-view comparison of the pre- and post-ExM images is shown in Figure 3B to illustrate the improvement in spatial resolution and contrast achieved *within* the sample of interest.

From the two-channel, pre- and post-ExM images, we consistently observed larger distortions both within and at the boundary of the nuclei—a feature that, to our knowledge, has not been reported in previous ExM studies. It is well known that the shape and volume of intact nuclei follow a non-linear relationship due to the restricted diffusion of solutes, particularly nucleic acid polymers across the nuclear

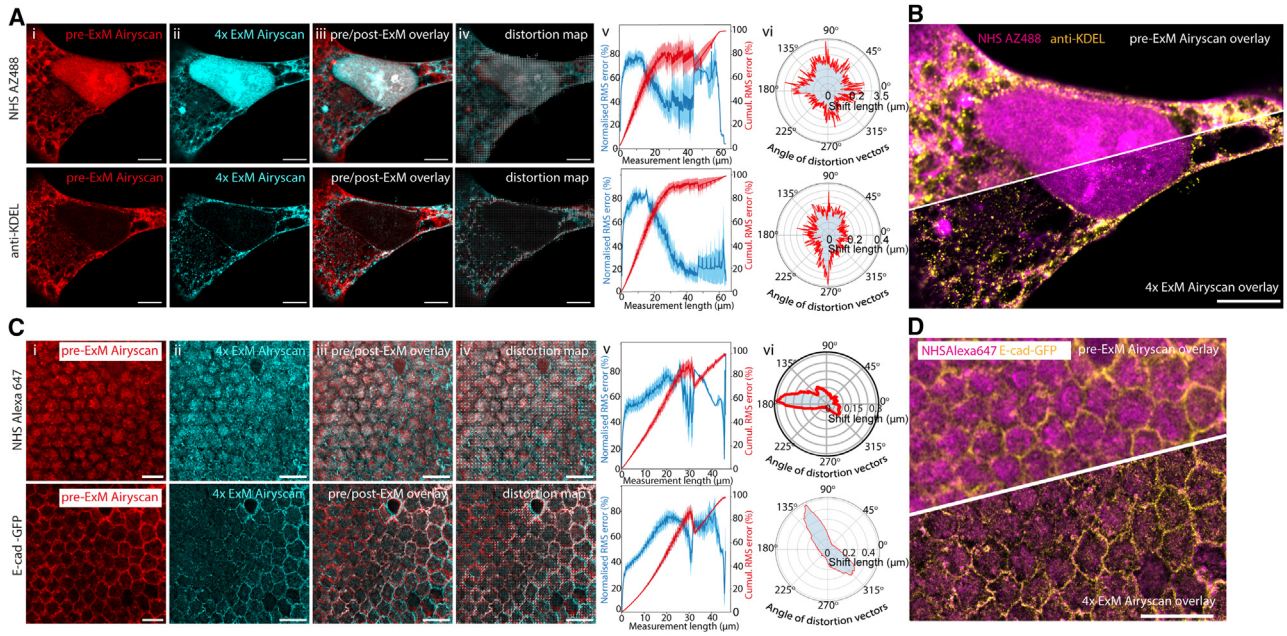

Figure 3. ***In situ*, pre-ExM and post-ExM multi-channel imaging of HeLa cells and fly wing tissue toward distortion assessment**

(A) A HeLa cell dual stained with AZ488 NHS ester (upper row) and anti-KDEL primary antibody (lower row). Shown, are (i) pre-ExM Airyscan, (ii) post-ExM Airyscan, (iii) overlay of pre- and post-ExM Airyscan images (pre-ExM in red and post-ExM in cyan), (iv) distortion map for each channel placed on the overlay in (iii), (v) RMSE (blue; averaged between eight image pairs from eight cells across four wells from two plates; light shading indicates SD), and normalized cumulative RMSE (red) plotted against measurement length scale, (vi) polar plots of the average distortion vectors (radial axis) against directionality (angular axis) in the distortion vector maps shown in the respective panels in (iv).

(B) Split view of the overlay of the AZ488 NHS ester (magenta) and anti-KDEL (yellow) imaged with Airyscan at pre-ExM and post-ExM stages.

(C) Equivalent views of an E-cad-GFP pupal wing tissue stained with Alexa 647 NHS ester (upper row) and anti-GFP targeting E-cad-GFP (lower). RMSE plots are averaged between nine image pairs from nine fly wing tissue samples; the averaged angular distortion polar plots were from the distortion vector map shown in the respective panels in (C, iv).

(D) Split view of the overlay of Alexa 647 NHS ester (magenta) and anti-GFP (E-cad) (yellow) imaged with Airyscan at pre-ExM and post-ExM stages. Scale bars, 5 μm (scale corrected by expansion factors in post-ExM images).

envelope.[28] It was likely that restricted access for the gel monomers across the nuclear envelope, despite permeabilization by the fixative, was causing distortions in the nucleoplasm or nuclear envelope. We therefore performed the same sequence of analyses as above on HeLa cells co-stained with AZ488 NHS ester and Nup98, a key component of the nuclear pore-complex residing in the nuclear envelope (see Figure S5). The distortion maps for both channels revealed prominent distortions both in the nucleoplasm and at the nuclear envelope, while the directionalities were matched between the distortions reported by the two independent channels (see polar plots in Figures S5Avi). Similar to the experiment presented in Figures 3A and 3B, the NHS ester stain paired with the anti-Nups98 demonstrated the utility of a widespread counterstain of the broader cellular ultrastructure for verifying the full extent of the distortions in the visualized image. We illustrate the visualization of pre- and post-4× ExM Airyscan images (Figures 3B and S5B) with the recommendation that ExM image data must not only display the resolution improvement, but also accompany channel-specific distortion vector maps as a part of responsible scientific practice. These examples also underscore the potential of multiplexed image data to independently verify regions exhibiting distortions through pre- and post-ExM imaging.

Tissue ExM is commonly prone to extensive distortions either due to heterogeneity in the hydrogel matrix and/or residual stiffness of the tissue. To study the nature of

these distortions, we performed two-color 4× ExM on E-cad-GFP *Drosophila* pupal wing tissues, stained and placed within the ExM microplate wells. Similar to two-color analysis of HeLa cells, we imaged NHS Alexa 647 (staining the full volume of each cell, across the tissue) and an anti-GFP antibody (localized at the E-cad junctions at the cell boundaries). While the distortion areas were larger in comparison with HeLa cells, a more systematic directionality to the distortion vectors was observed both visually (in the distortion maps in Figure 3Civ) and statistically (in polar plots in Figures 3Cvi). The greater coverage and density of staining across the tissue of the NHS Alexa 647 compared with antibodies, lent toward a more complete, macroscale distortion vector map (Figure 3Civ; see higher-resolution versions in Figures S6 and S7). The notable limitation of the use of NHS ester staining, however, is the loss of contrast of the intracellular (nanoscale) ultrastructure, by comparison with cultured cells. This can limit the usable intrinsic alignment fiducials between pre- and post-ExM images to macroscale features such as the cell outlines. In the fly wing tissue example presented (see higher-resolution versions in Figure S6), the linearity of the NHS ester staining densities also modestly shifted from largely intracellular staining (red channel) to accentuated cell boundaries (cyan) post-ExM. This is a likely co-lateral effect of bleaching and loss of intrinsic proteins resulting from the digestion step of the ExM protocol. While the NHS ester stain images still allowed us to perform a macro-scale (i.e., tissue-wide) distortion analysis, choosing a robust and high-contrast NHS ester stain that highlights the cellular structures of interest (as evaluated previously[27]) can minimize this effect.

Further considerations on hydrogel-dependent distortions in ExM

Furthermore, we considered the determinants of the distortions and aberrations in ExM imaging. A drop in the fluorescence density in the sample is inherent to all ExM samples. In pre- and post-ExM imaging performed in microplates using 40× water (NA 1.2) and oil immersion (NA 1.3), objective lenses produce near-identical reductions in the signal-to-noise ratio of the images (Figure S8). While we chose the lenses with higher numerical aperture to maximize light collection, the worse refractive index matching manifested in a slightly more blurry image, particularly in pre-ExM imaging. The distortions that we observed also depended on the step of the ExM protocol when the sample is imaged. Exploiting the ability to track the sample at any time point of the protocol with the microplate-based imaging, we performed repeated imaging of HeLa cells at pre-digestion, post-digestion, and post-expansion time points (Figure S9). Distortion analyses revealed regions with the proportionally largest distortions between the pre- and post-digestion time points (see Figure S9D). This comparison point also featured a modest expansion of the sample (by a factor of ∼1.5). The post-digestion and post-expansion (hydration) yielded a further expansion factor of ∼2.5 and smaller distortion vectors relative to the new dimensions of the cells. Based on these observations, we identify the digestion/denaturation step as the primary cause of distortions in cell ExM.

Can the nano-micron scale distortions observed with this method be corrected post-hoc? The B-spline transformations generated in the re-scaling and alignment of image pairs provide a possible pathway to achieving this. Figure S10 illustrates two examples of distortion corrections attempted using B-spline grids of different pixel sizes (see supplemental section 2.5 for method). While re-alignment of the major structural features was achieved, the lack of regularization of diffraction-limited features of the post-ExM images appeared to compromise both their shapes and sizes in the output image. From this analysis, we further conclude that the fidelity of both the B-spline grids (and therefore distortion detection), as well as any distortion correction, is limited by the resolution of the pre-ExM image. Cellular or

tissue-level distortions detected with the approach presented here, in our view, are more useful for informing the limitations of ExM images and data curation rather than image restoration.

As a rapidly evolving bio-imaging technique, ExM continues to improve in its versatility and compatibility with various sample types. The microplate-based approach, by helping preserve the geometry and contain the ExM sample processing pipeline, will improve convenience and the ability to perform pre- and post-ExM imaging. Its compatibility with both cell samples and tissue samples will allow its adaptation for high-resolution medical/biopsy imaging[29] as well as imaging complex, multicellular organisms,[19] organs, or tissues.[30] While the microplate approach presented in this paper can be viewed as a gateway to improving throughput, our experience is that the fragility of polyacrylamide gels still requires a level of care, skill, and attention that may yet be prohibitive for large sample numbers or automation. As the precision of prototyping continues to improve, we anticipate adaptations of bespoke ExM microplates and more precise frame inserts to extend to recipes with larger expansion factors on offer.

Numerous types of artifacts, arising from the reliance of tissue digestion/denaturation as well as the flexibility, heterogeneity, and phase separation of the hydrogel polymers are intrinsic to ExM.[25] It is the responsibility of the investigators to characterize and document these errors in the context of the spatial features of the images. While some artifacts such as fracturing and shearing are detectable by investigators with no additional tools, a quantitative approach using pre- and post-ExM distortion analysis reveals artifacts not detected by examining post-ExM images alone (e.g., Figure 2G). Our data show that these distortions can occur in sub-cellular regions that include boundaries of organelles or edges of cells that can alter the proportions of organelles such as nuclei. In tissue ExM (Figure 2L), multi-cellular regions can be subjected to warping, shearing, or tilting, which can alter any spatial measurements of cell sizes or shapes. Performing pre- and post-ExM imaging on every sample would provide an assurance against such distortions; however, the process of repeated imaging has been discussed frequently in ExM user groups as laborious and time consuming. The geometry preserving microplates and the spacer inserts provide a useful strategy to both constraining the ExM experiment to one array and coordinate-based repeated imaging. Other approaches that include image alignment by sample geometry[31] or grid patterns imprinted to the hydrogel[24] also provide pathways to repeated imaging and image registration. The advantage of using the intrinsic ultrastructure of a pre-ExM image, as in our study, is that localized distortions can be detected without being limited to the grid size or the overall dimensions of the sample. However, an amalgamation of all of these tools will perhaps offer the greatest precision of any distortion analyses. While image restoration tools are still limited to the resolution of the diffraction-limited image or the fiducial grids, excluding images or sub-regions with large distortions (e.g., regions with distortion vectors $\gtrsim$ 200% of the optical resolution) from all post-hoc analyses would constitute best practice in the short term.

Finally, the experiments presented in this paper leverage pro-ExM with a nominal 4-fold expansion recipe. Numerous recipes enabling greater expansion factors (e.g., U-ExM[5] and X10 ExM[3]) are now in broad use. To adopt the geometry preserving pre- and post-ExM imaging with these recipes, we propose two possible strategies. The first is a modification of the CAD model of the plates and silicone frame insert provided in the data supplement to achieve a 10-fold difference between the dimensions of the central well of the inserts and the dimensions of the plate's well.

The dimensions of these objects are easily scalable with common CAD software such as Autodesk Fusion 360. Higher-resolution fabrication methods such as soft lithography with a material similar to polydimethylsiloxane and focused ion beam micromachining may be necessary for manufacturing frame inserts with finer central wells. The second strategy that we propose is to adopt an outer frame insert that is permanently mounted within round/petri dishes or 6-well microplate chambers that will trap the (inner) frame insert. Similar to the first strategy, the inner frame insert could be rescaled to allow a 10-fold difference in the size between pre- and post-expansion gels.

EXPERIMENTAL PROCEDURES

Resource availability

Lead contact

Further information and requests for resources and reagents should be directed to and will be fulfilled by the lead contact, Izzy Jayasinghe via (i.jayasinghe@sheffield.ac.uk).

Material availability

This study generated new microplates and frame inserts. At the time of publication, these have not been made available commercially. Please refer to the resource availability section for details on accessing the CAD files. HeLa-CCL2 cells (human cervix epithelioid carcinoma) used for this study were gifted to us by the Department of Infection, Immunity and Cardiovascular Disease, Medical School, University of Sheffield, Beech Hill Rd, Sheffield S10 2RX. All other materials are listed below and are commercially available for purchase.

Data and code availability

The Python code, along with example datasets, are included in the data supplement, accessible at https://doi.org/10.5281/zenodo.8381689. Also included in this data supplement are the.stl versions of the microplate and the frame inserts.

Microplates and frame inserts

Both the microplate and the inserts were designed using Autodesk Fusion360 software and exported as a.stl files. The microplate.stl CAD file was sliced using Chitubox Basic v.1.9.0 slicer software and fabricated using an Elegoo Saturn 2 SLA 3D printer using translucent photopolymer resin (Elegoo) at 100% infill, 50 μm layer thickness, 5 bottom layers, 3.0 s standard exposure times, and 20 s bottom layer exposure time. We have also reproduced qualitatively similar results with printing the same CAD file with Snapmaker 2.0 3D printer, sliced with Cura v.5.0 (Ultimaker), standard black acrylonitrile butadiene styrene filament (Protopasta) at 0.24 mm layer height, 18% infill density, 2 mm wall thickness, printing temperature of 245°C, and bed temperature of 80°C. Number 1.5 coverslips, sized 22 × 22 mm (Menzel-Glaser, Germany) were adhered to the bottom using epoxy glass glue (Araldite) and cured under a UV hood. Frame inserts were fabricated with laser CNC from black, autoclavable silicone sheet rubber with a 3 mm thickness (custom ordered via Laser Web).

Cell culture

HeLa cells were cultured in DMEM with high glucose, L-glutamine, HEPES, Phenol Red (Fisher Scientific, UK), and 10% fetal bovine serum (v/v; LabTech International, UK), supplemented with 1% penicillin-streptomycin (v/v; containing 10,000 units/mL of penicillin and 10,000 μg/mL of streptomycin in a 10 mM citrate buffer; Fisher

Scientific). Cells were incubated at 37°C and 5% CO_2 as standard and were used once the samples reached ~70%–80% confluency, typically 2 days after passage.

Prior to cell seeding, the full chambers were sterilized through 70% ethanol (v/v) spray down and then UV irradiation for 1 h. The coverslip bottom of each well (pre-attached to the ExM plate) was coated with 0.01 mg/mL poly-D-lysine (code: 3439-100-01, Cultrex) for 2 h at 37°C and 5% CO_2. After removing the excess, cells were detached via 0.05% Trypsin-EDTA (Gibco, Fisher Scientific), spun at 400 × *g* for 5 min and resuspended in fresh medium and then seeded at a density of 75,000/mL (1 mL of the passaged mixture). Cell suspensions were kept in culture at 37°C and 5% CO_2, with daily medium replacement until use after 2 days.

D. melanogaster model for tissue ExM experiments

D. melanogaster flies from strain *shg*:E-cad-GFP (FlyBase: FBti0168565; RRID: BDSC_60584; Bloomington stock no. 60584), sourced from Bloomington Drosophila Stock Center, were grown on standard cornmeal/agar/molasses medium at 25°C.

Immunofluorescence cytochemistry of HeLa cells

Fixation of HeLa cells was performed 2 days after plating in 2% paraformaldehyde (PFA) (1 mL of 4% PFA diluted in 1 mL fresh medium and for final concentration of 2%) for 10 min. Followed by 3 × 10-min washes in fresh phosphate-buffered saline (PBS). Cells were stored in PBS containing 0.5% bovine serum albumin (w/v) and 0.1% sodium azide (w/v) at 4°C until the immunostaining steps.

At use, cells were permeabilized in PBS (137 mM NaCl, 2.7 mM KCl, 10 mM Na_2KPO_4, 2 mM KH_2PO_4 [pH 7.3]) + 0.1% (v/v) Triton X-100, and subsequently blocked in PBS + 10% normal goat serum (NGS) (v/v) + 0.05% Triton X-100.

Immunostaining was carried out in antibody incubation solution containing 0.05% Triton and 2% NGS in PBS with the addition of 200 µL primary antibody added to each well before incubation at 4°C overnight. The samples were then washed with fresh PBS 3 times in 5-min steps prior to secondary antibody application in 200 µL for 2 h at room temperature. The samples were then washed in fresh PBS 3 times in 20-min steps.

For NHS ester application, after permeabilizing the cells, 200 µL of 1:1,000 NHS ester in ester staining solution (100 mM $NaHCO_3$ + 1 M NaCl [pH 6] made up to 100 mL with dH_2O) was added per well for 90 min at room temperature. Samples were washed 3 times with PBS in 20-min steps prior to the blocking step.

Immunofluorescence histochemistry of fly wings

Drosophila pupal wings were dissected at 28 h after puparium formation at 25°C. Pupae were stuck down and the cuticle removed. Pupae were placed in a drop of 4% PFA in PBS and fixed for 30 min at room temperature prior to dissection of the pupal wing from the pupal carcass and fixed for another 10 min before removing the inner cuticle.

For staining, wings were transferred into PBS and permeabilized for 30 min in 1× PBS + 0.1% Triton X-100 (v/v; PTX). Alexa 647 NHS ester 1:200 in 1× PBS was added for 1 h. Samples were washed in 1× PBS and blocked in 0.1% Triton X-100 and 10% normal goat serum (Jackson Laboratories) prior to antibody incubation. Wings were incubated with 1:200 affinity-purified rabbit anti-GFP (ab6556, Abcam, UK) in PBS with 10% normal goat serum (v/w) overnight at 4°C. Washes were in PBS. Then,

Table 1. Antibodies and fluorescent dye ester probes used for sample labeling and other materials used for developing the experiments of this paper

Esters	Catalog no.	Supplier	Dilution of stock
NHS AZ488	1013-1	Fluoroprobes	1:1,000
NHS Alexa 488	A20000	Thermo Fisher Scientific	1:1,000
NHS Alexa 647	A20006	Thermo Fisher Scientific	1:1,000
Primary antibodies			
Anti-KDEL (rabbit)	PA1-013	Thermo Fisher Scientific	1:500
Anti-Nup98 (mouse)	sc-74578	Santa Cruz	1:200
Anti-GFP, affinity purified (rabbit)	ab6556	Abcam	1:200
Secondary antibodies			
Alexa Fluor 594 goat anti-rabbit	A11012	Thermo Fisher Scientific	1:200
Alexa Fluor 594 goat anti-mouse	A11005	Thermo Fisher Scientific	1:200

incubation was carried out with anti-rabbit Alexa Fluor 488 (Thermo Fisher Scientific) for 4 h at room temperature. After immunostaining wings were post-fixed in 4% PFA in PBS for 10 min and washed in 1× PBS. Stained wings were placed on the expansion plate and allowed to slightly air dry to adhere to the bottom of the well before carrying out the plate-based 4× ExM protocol (below).

All the antibodies and NHS esters used for the fluorescent staining are summarized in Table 1.

Anchoring

Fluorophores were prepared for linking into the gel by incubating them at 4°C overnight in 250 μL of PBS and 1% Acryloyl-X (w/v; catalog no. A20770, Fisher Scientific).

4× gel preparation

Cells or tissue samples in each well were washed with PBS 3 times in 20-min steps. They were incubated in 200 μL of monomer solution (sodium acrylate, acrylamide, MBAA, NaCl, PBS, dH_2O) for 30 min at 4°C. The monomer solution was removed and the Frame inserts were assembled into each well, ensuring that they were in good contact with the coverslip. A 4× gel solution (100 μL; containing 297 μL monomer solution, 6 μL 10% TMED, 6 μL 10% APS, 6 μL PBS) was added to the center of each frame. The 10% APS and 10% TMED components were added to the gel mix immediately prior to dispensing into the wells to minimize pre-polymerization of the gel before monomers were delivered into the cells. The plate was covered with either a bespoke lid or the lid of a 6-well plate allowing time for gel polymerization. The plate was incubated at 37°C for 2 h. Video S1 contains a brief video demonstration of the gelation within the microplate well.

4× ExM gel digestion and expansion

The frame inserts were gently removed from the wells with the aid of a tweezer, being careful in rare cases of gel adhering to the frames. Digestion buffer (1 mL; containing 50 mM Tris, 1 mM EDTA, 0.5% Triton + 0.8 M guanidine HCl, made up to 100 mL with dH_2O) along with 1% proteinase K (w/v; Sigma-Aldrich) was then added to each well and incubated on a rocker overnight at room temperature. Digestion was performed for at least 12 h, with shorter times known to lead to gel damage. Each digested sample had an excess of dH_2O to allow expansion while fully immersed. The dH_2O was replaced at least 3 times, with 1 h for each stage of expansion until approximately ~4-fold expansion was achieved, i.e., until the gel reached the edges of the well.

The digestion buffer incubation time was adjusted to 5 h for the fly wing ExM samples.

Imaging

All images were obtained on a Zeiss LSM880 AiryScan (Carl Zeiss, Jena, Germany), using a 10× 0.3 NA air Plan Apochromat objective and a 40× 1.3 NA oil-immersion Plan Apochromat objective (both from Carl Zeiss). Imaging was performed in Airyscan mode with the gain and laser power adjusted for each sample to accommodate the fluorescence reduction occurring due to the spatial separation of fluorophores during expansion. Fluorophores were excited using argon 488 nm and DPSS 561 nm laser lines. Selection of emission bands was performed through the spectral detector and recorded with the in-built GaAsP detector. Image acquisition was done through the associated Zen software and passed through the Airyscan post-hoc processing to obtain the final image.

Image analysis

Three avenues of image analysis were performed: pre- and post-expansion image alignment using ImageJ, distortion mapping using adjusted Python code from Truckenbrodt et al.[25] (available via https://github.com/sommerc/expansion_factor_bftm), and RMSE data acquisition and plotting through a custom-written Python code. See Video S2 for a screencast of the analysis of pre- and post-ExM image alignment. A written protocol of the full analysis, including the distortion maps and RMSE estimation is included in supplemental section 2. All image analysis steps were carried out in a 13″ MacBook Pro (Apple) with an Intel 1.7 GHz dual-core processor, 16 Gb of memory, and 256 Gb in SSD storage.

Pre- and post-ExM image alignment

Pre- and post-ExM images were aligned through the ImageJ plugin, Linear Stack Alignment with SIFT, with the transformation matrix visible. The intrinsic expansion factor (specific to the region of interest) was one of the outputs generated from the transformation matrix.

Distortion analysis

The pre-ExM image was upscaled based on the estimated intrinsic expansion factor. Using the aligned image set, we determined the relative shift in coordinates of features present in the upscaled pre- and post-ExM images. The Farnebäck optical flow algorithm[32] was used to assess the relative shift between these images in this step, as detailed previously by Truckenbrodt et al.[25] The output from this was used to produce distortion maps for the region of interest.

Using the aligned dataset, Otsu thresholding was performed on the post-expansion image to generate a binary image highlighting feature coordinates in the structure. The respective theoretical post alignment coordinates were then produced from the optical flow output respective to the feature coordinates. This series of theoretical "expanded," pre-expansion coordinates, and actual post-expansion coordinates were grouped by nearest neighbor distance. Nearest neighbor distance between the paired feature coordinates was subtracted to obtain the associated difference between the length measurements. The original length between the coordinate points and the difference value were necessary to obtain the RMSE. Subsequently, the binarized images were binned iteratively and the RMSE calculated for each difference value set associated with a bin position. In each iteration, the binning was adjusted to a pixel size that represented the length scale the RMSE was recorded against. In RMSE plots shown in Figures 2 and 3, the "measurement length scale" is the bin size used for calculating each RMSE value. The scaling used for the bin size was the true image pixel scale (uncorrected for the expansion factor). The RMSE plots shown in Figures 2 and 3 were constructed by averaging multiple RMSE curves constructed from multiple unique datasets (see n numbers in Table S1).

The polar plots of the average angular distortion vector length were generated using the output from the optical flow algorithm and the produced vectors (see above).

The aligned images were commonly of size ~2,550 × 2,550 pixels, hence the sequence of Otsu thresholding, erosion, and closing, and the subsequent skeletonization of the binary image helped to reduce the 6 million+ image pixels to a range of 30,000–200,000. The skeletonization also allowed for RMSE calculations to be constrained to regions that recorded a detectable pixel value above the typical background (i.e., regions with positive labeling).

All post-ExM images shown in the paper have been displayed with a scale bar corrected for the expansion factor estimated with this method. The average expansion factors estimated through the multi-time point image scaling and alignment are summarized, along with sample numbers used, are listed in Table S1.

SUPPLEMENTAL INFORMATION

Supplemental information can be found online at https://doi.org/10.1016/j.xcrp.2023.101719.

ACKNOWLEDGMENTS

The biological samples demonstrating the methodology were all from the HeLa cell line. Henrietta Lacks, and the HeLa cell line that was established from her tumor cells without her knowledge or consent in 1951, have made significant contributions to scientific progress and advances in human health. The authors are grateful to Henrietta Lacks, now deceased, and to her surviving family members for their contributions to biomedical research. The authors thank the reviewers whose feedback has helped improve this paper substantially. This research was funded by the UK Research and Innovation, United Kingdom (MR/S03241X/1), and studentship from the Engineering and Physical Sciences Council. S.J.W. and D.S. were funded by a Wellcome Trust Senior Fellowship to D.S. (210630/Z/18/Z). The authors acknowledge the Wolfson Light Microscopy Facility at the University of Sheffield, United Kingdom, where all the imaging was performed, and Dr Wendy Lawley who facilitated the collaborations that underpin this study.

AUTHOR CONTRIBUTIONS

I.J. secured the primary funding and conceived the concept. I.J., R.S.S., and S.J.W. designed the experiments tools. I.J. and R.S.S. performed the manufacturing of the tools. R.S.S., S.J.W., and B.H.K.A. performed the experiments. T.S., M.E.S., and S.J.W. provided the material. T.M.D.S., D.B., D.S., A.C., and I.J. provided supervision. R.S.S. and I.J. performed the data analysis. I.J., R.S.S., and S.J.W. wrote the manuscript. All authors reviewed and refined the manuscript.

DECLARATION OF INTERESTS

We have begun the proceedings to file for a patent application relating to the bespoke microplates and frame-based ExM concept. I.J. is a member of the advisory board for *Cell Reports Physical Science*.

Received: February 22, 2023
Revised: September 27, 2023
Accepted: November 8, 2023
Published: December 4, 2023

REFERENCES

1. Chen, F., Tillberg, P.W., and Boyden, E.S. (2015). Optical imaging. Expansion microscopy. Science *347*, 543–548.
2. Tillberg, P.W., Chen, F., Piatkevich, K.D., Zhao, Y., Yu, C.C.J., English, B.P., Gao, L., Martorell, A., Suk, H.J., Yoshida, F., et al. (2016). Protein-retention expansion microscopy of cells and tissues labeled using standard fluorescent proteins and antibodies. Nat. Biotechnol. *34*, 987–992.
3. Truckenbrodt, S., Maidorn, M., Crzan, D., Wildhagen, H., Kabatas, S., and Rizzoli, S.O. (2018). X10 expansion microscopy enables 25-nm resolution on conventional microscopes. EMBO Rep. *19*, e45836.
4. Damstra, H.G.J., Mohar, B., Eddison, M., Akhmanova, A., Kapitein, L.C., and Tillberg, P.W. (2022). Visualizing cellular and tissue ultrastructure using Ten-fold Robust Expansion Microscopy (TREx). Elife *11*, e73775.
5. Gambarotto, D., Hamel, V., and Guichard, P. (2021). Ultrastructure expansion microscopy (U-ExM). Methods Cell Biol. *161*, 57–81.
6. Lee, H., Yu, C.C., Boyden, E.S., Zhuang, X., and Kosuri, P. (2021). Tetra-gel enables superior accuracy in combined super-resolution imaging and expansion microscopy. Sci. Rep. *11*, 16944.
7. Hawkins, T.J., Robson, J.L., Cole, B., and Bush, S.J. (2023). Expansion Microscopy of Plant Cells (PlantExM). Methods Mol. Biol. *2604*, 127–142.
8. Cho, I., and Chang, J.B. (2022). Simultaneous expansion microscopy imaging of proteins and mRNAs via dual-ExM. Sci. Rep. *12*, 3360.
9. White, B.M., Kumar, P., Conwell, A.N., Wu, K., and Baskin, J.M. (2022). Lipid Expansion Microscopy. J. Am. Chem. Soc. *144*, 18212–18217.
10. Steib, E., Tetley, R., Laine, R.F., Norris, D.P., Mao, Y., and Vermot, J. (2022). TissUExM enables quantitative ultrastructural analysis in whole vertebrate embryos by expansion microscopy. Cell Rep. Methods *2*, 100311.
11. Gao, M., Maraspini, R., Beutel, O., Zehtabian, A., Eickholt, B., Honigmann, A., and Ewers, H. (2018). Expansion Stimulated Emission Depletion Microscopy (ExSTED). ACS Nano *12*, 4178–4185.
12. Halpern, A.R., Alas, G.C.M., Chozinski, T.J., Paredez, A.R., and Vaughan, J.C. (2017). Hybrid Structured Illumination Expansion Microscopy Reveals Microbial Cytoskeleton Organization. ACS Nano *11*, 12677–12686.
13. Zwettler, F.U., Reinhard, S., Gambarotto, D., Bell, T.D.M., Hamel, V., Guichard, P., and Sauer, M. (2020). Molecular resolution imaging by post-labeling expansion single-molecule localization microscopy (Ex-SMLM). Nat. Commun. *11*, 3388.
14. Sheard, T.M.D., Hurley, M.E., Colyer, J., White, E., Norman, R., Pervolaraki, E., Narayanasamy, K.K., Hou, Y., Kirton, H.M., Yang, Z., et al. (2019). Three-Dimensional and Chemical Mapping of Intracellular Signaling Nanodomains in Health and Disease with Enhanced Expansion Microscopy. ACS Nano *13*, 2143–2157.
15. Sheard, T.M.D., Hurley, M.E., Smith, A.J., Colyer, J., White, E., and Jayasinghe, I. (2022). Three-dimensional visualization of the cardiac ryanodine receptor clusters and the molecular-scale fraying of dyads. Philos. Trans. R. Soc. Lond. B Biol. Sci. *377*, 20210316.
16. Shaib, A.H., Chouaib, A.A., Imani, V., Chowdhury, R., Georgiev, S.V., Mougios, N., Monga, M., Reshetniak, S., Mihaylov, D., Chen, H., et al. (2022). Expansion microscopy at one nanometer resolution. Preprint at bioRxiv.
17. Karagiannis, E.D., Kang, J.S., Shin, T.W., Emenari, A., Asano, S., Lin, L., Costa, E.K., Marblestone, A.H., Kasthuri, N., and Boyden, E.S. (2019). Expansion Microscopy of Lipid Membranes. Preprint at bioRxiv, 829903.
18. M'Saad, O., and Bewersdorf, J. (2020). Light microscopy of proteins in their ultrastructural context. Nat. Commun. *11*, 3850.
19. Sim, J., Park, C.E., Cho, I., Min, K., Eom, M., Han, S., Jeon, H., Cho, H.-J., Cho, E.-S., Kumar, A., et al. (2022). Nanoscale resolution imaging of the whole mouse embryos and larval zebrafish using expansion microscopy. Prepritn at. bioRxiv.
20. Konigshausen, E., Schmitz, C.T., Rump, L.C., and Sellin, L. (2021). Imaging of Podocytic Proteins Nephrin, Actin, and Podocin with Expansion Microscopy. J. Vis. Exp.
21. Gambarotto, D., Zwettler, F.U., Le Guennec, M., Schmidt-Cernohorska, M., Fortun, D., Borgers, S., Heine, J., Schloetel, J.G., Reuss, M., Unser, M., et al. (2019). Imaging cellular ultrastructures using expansion microscopy (U-ExM). Nat. Methods *16*, 71–74.
22. Pesce, L., Cozzolino, M., Lanzanò, L., Diaspro, A., and Bianchini, P. (2019). Measuring expansion from macro- to nanoscale using NPC as intrinsic reporter. J. Biophot. *12*, e201900018.
23. Vanheusden, M., Vitale, R., Camacho, R., Janssen, K.P.F., Acke, A., Rocha, S., and Hofkens, J. (2020). Fluorescence Photobleaching as an Intrinsic Tool to Quantify the 3D Expansion Factor of Biological Samples in Expansion Microscopy. ACS Omega *5*, 6792–6799.
24. Damstra, H.G.J., Passmore, J.B., Serweta, A.K., Koutlas, I., Burute, M., Meye, F.J., Akhmanova, A., and Kapitein, L.C. (2023). GelMap: intrinsic calibration and deformation mapping for expansion microscopy. Nat. Methods *20*, 1573–1580.
25. Truckenbrodt, S., Sommer, C., Rizzoli, S.O., and Danzl, J.G. (2019). A practical guide to optimization in X10 expansion microscopy. Nat. Protoc. *14*, 832–863.
26. Day, J.H., Maretich, P., Santina, C.M.D., Auld, A.L., Shin, T., Boyden, E.S., and Boyer, L.A. (2023). HiExM: high-throughput expansion microscopy enables scalable super-resolution imaging. Preprint at bioRxiv.
27. Sheard, T.M.D., Shakespeare, T., Seehra, R.S., Spencer, M.E., Suen, K.M., and Jayasinghe, I. (2023). Differential labelling of human sub-cellular compartments with fluorescent dye esters and expansion microscopy. Preprint at bioRxiv.
28. Finan, J.D., Chalut, K.J., Wax, A., and Guilak, F. (2009). Nonlinear osmotic properties of the cell nucleus. Ann. Biomed. Eng. *37*, 477–491.
29. Zhao, Y., Bucur, O., Irshad, H., Chen, F., Weins, A., Stancu, A.L., Oh, E.Y., DiStasio, M., Torous, V., Glass, B., et al. (2017). Nanoscale imaging of clinical specimens using pathology-optimized expansion microscopy. Nat. Biotechnol. *35*, 757–764.
30. Suen, K.M., Sheard, T.M., Lin, C.C., Milonaityte, D., Jayasinghe, I., and Ladbury, J.E. (2023). Expansion microscopy reveals subdomains in C. elegans germ granules. Life Sci. Alliance *6*, e202201650.
31. Zhu, C., Wang, A., Chen, L., Guo, L., Ye, J., Chen, Q., Wang, Q., Yao, G., Xia, Q., Cai, T., et al. (2021). Measurement of expansion factor and distortion for expansion microscopy using isolated renal glomeruli as landmarks. J. Biophot. *14*, e202100001.
32. Farnebäck, G. (2003). Two-Frame Motion Estimation Based on Polynomial Expansion, J. Bigun and T. Gustavsson, eds. (Springer Berlin Heidelberg), pp. 363–370. held in Berlin.